

Fourier Electron Optics with Massless Dirac Fermions Scattered by Quantum Dot Lattice

Partha Sarathi Banerjee, Rahul Marathe, and Sankalpa Ghosh

Department of Physics, Indian Institute of Technology Delhi, Hauz Khas, New Delhi 110016

(Dated: February 17, 2024)

The field of electron optics exploits the analogy between the movement of electrons or charged quasiparticles, primarily in two-dimensional materials subjected to electric and magnetic (EM) fields and the propagation of electromagnetic waves in a dielectric medium with varied refractive index. We significantly extend this analogy by introducing Fourier electron optics (FEO) with massless Dirac fermions (MDF), namely the charge carriers of single-layer graphene under ambient conditions, by considering their scattering from a two-dimensional quantum dot lattice (TDQDL) treated within Lippmann-Schwinger formalism. By considering the scattering of MDF from TDQDL with a cavity, as well as the moiré pattern of twisted TDQDLs, we establish an electronic analogue of Babinet's principle in optics. Exploiting the similarity of the resulting differential scattering cross-section with the Fraunhofer diffraction pattern, we construct a dictionary for such FEO. Subsequently, we evaluate the resistivity of such scattered MDF using the Boltzmann approach as a function of the angle made between the direction of propagation of these charge-carriers and the symmetry axis of the dot-lattice, and Fourier analyze them to show that the spatial frequency associated with the angle-resolved resistivity gets filtered according to the structural changes in the dot lattice, indicating wider applicability of FEO of MDF.

The unique transmission properties of massless Dirac fermions (MDF) in graphene through potential landscapes created by a variety of electromagnetic (EM) fields, particularly in the ballistic regime[1–6], and its similarity with the light transmission through an optical medium with unconventional dielectric properties such as metamaterials[7, 8] make graphene an excellent material to realize electron optics-based devices in a solid state system. The realisation of negative refraction [9], chiral Veselago lensing of MDF in two[10] and three dimensions [11], tunable Veselago interference in a bipolar graphene microcavity[12], creation of a Dirac fermion microscope [13], collimation [14–16], and different type of interferometers [17–20], gate tunable beam-splitter of such MDF [21], Fabry-pérot resonator in graphene/hBN moiré super-lattice [22], gradient index electron optics in graphene p-n junction [23], Mie scattering in graphene, [24] are few milestones in this direction. Most of these experimental and theoretical studies are based on theoretical modelling of Dirac fermions scattered by the potential, which are constant in one direction [1–6, 14, 25, 26], and hence limit the range of applications in this fast-growing field.

New possibilities can emerge if the EM potential that can scatter such MDF can vary along both directions in a two-dimensional plane. For example, in the well-known Fraunhofer diffraction, when the observation point is significantly distant(z) from the diffracting object dubbed as the far-field case, the field distribution at the observation plane is the Fourier transform of the aperture function($A(x', y')$)[27–32]. The diffracting object is positioned at the back focal length of a lens, resulting in the generation of an image at the front focal length of the lens, thereby satisfying the conditions for the Fraunhofer approximation($z \gg [x'^2 + y'^2]_{\max} / \lambda$) as depicted in FIG. 1 and described in TABLE I. In this work we

show that an electronic analogue of this situation can be realized in a fully two-dimensional (2D) scattering model, where the scattering of such MDF takes place from a two-dimensional superlattice potential that can be realised by creating an electrostatically defined array of quantum dots (QDs) on the surface of single-layer graphene [33–40].

Particularly in the ballistic regime, with the Fermi velocity $v_F \sim 10^6$ m s⁻¹, the mean free path of the charge carriers in graphene are several microns[41–43] \gg the size of (~ 10 nm)[44] such scatterers, and the Fraunhofer criterion is satisfied [43, 45, 46]. The visibility criteria for observing a clear diffraction pattern in optical case[31, 32], which is ensured by making the length of the aperture comparable with the wavelength of light, can be implemented by considering the lattice spacing(~ 40 nm) and characteristic length(~ 10 nm) of each barrier[44] in this QD lattice smaller than the de Broglie wavelength calculated from the incident energy of the graphene electrons ($\sim 30 - 40$ meV)[20]. Also, for the typical energy range we have considered, the wavevector of the MDF is much smaller than the Fermi wave vector, i.e., $k \ll k_F$, eliminating the possibility of inter-valley scattering. Thus, the problem can be modelled by starting with the single-valley non-interacting Hamiltonian of the massless Dirac fermions in single-layer graphene given by $\hat{H}_0 = v_F \sigma \cdot \mathbf{p}$. Such a two-dimensional QD lattice (TDQDL) serves as two-dimensional grating for the incident charge carriers for graphene, leading to an electronic analogue of Fraunhofer diffraction pattern, but with an important distinction characterising the absence of backscattering for such MDF[47, 48].

The scattered state of such MDF $|\Psi_{\mathbf{k}}\rangle$ from an arbitrary scattering potential V can be obtained by finding out the solutions of $(\hat{H}_0 + \hat{V})|\Psi_{\mathbf{k}}\rangle = E|\Psi_{\mathbf{k}}\rangle$ using the Lippmann-Schwinger formalism and can be written as

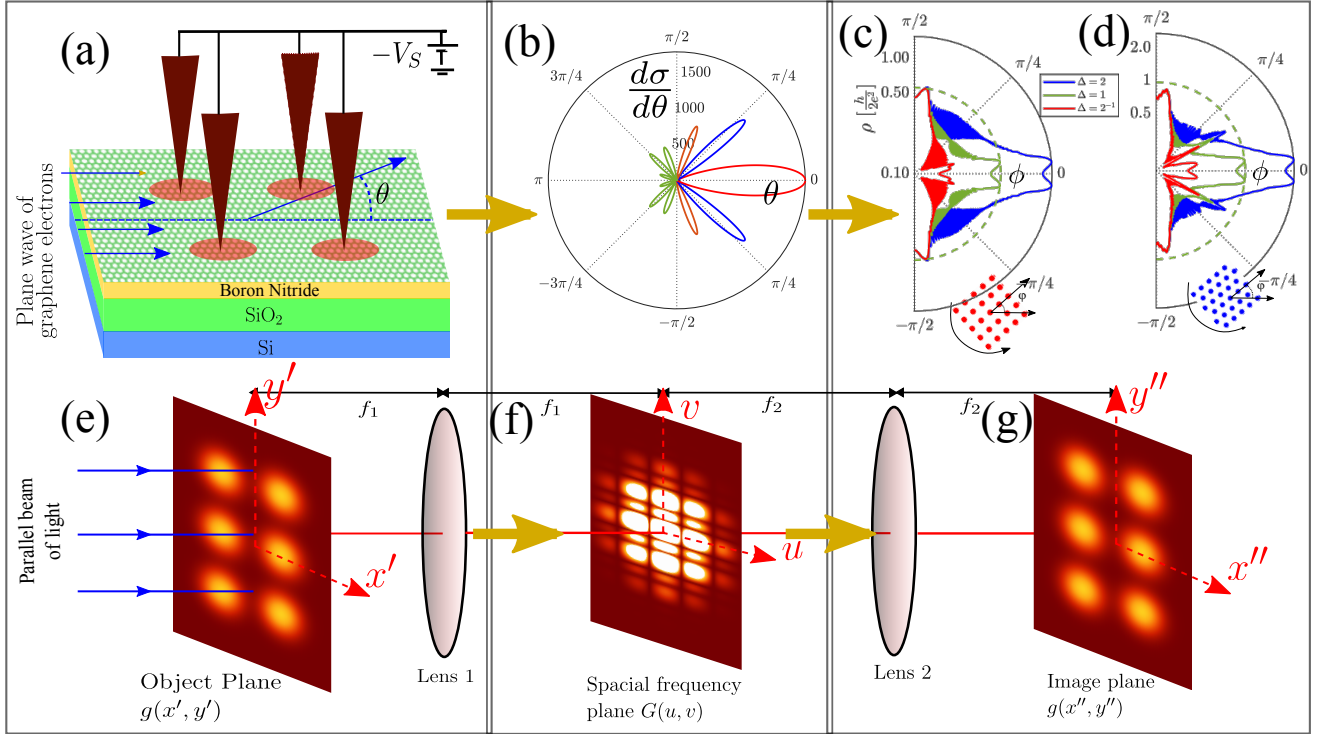


FIG. 1: (a) The schematic diagram of a plane wave (direction shown in blue arrows) of charge carriers in ballistic graphene that are modelled as MDF under ambient conditions, getting scattered by a two-dimensional array of Gaussian quantum dot(QD) potentials created by STM tips. (b) The polar plot of the DSC for a square lattice of QDs as given by Eq. (3a), of dimension $N_1 = 10, N_2 = 0$ and orientation $\phi = 0$. For better visibility, the central maxima at $\theta = 0$ is multiplied with 1.6×10^{-3} . The first maximas on both sides are multiplied by 0.8×10^{-2} . The second ones are multiplied by 0.32 for better visibility with respect to the other smaller peaks. (c) and (d) plotted the angle-resolved dc-resistivity of the system parallel to the direction of propagation of the incoming plane wave of graphene electrons under this scattering potential rotated at an arbitrary angle. The resistivity pattern for square and hexagonal lattices of QDs is shown in (c) and (d) for $N_2 = 100$. The resistivity at $\phi = 0^\circ$ and 90° is the same for the square lattice but not in the case of the hexagonal lattice. In Figs. (e)-(g) we compare the process described in (a)-(d) with the two-dimensional optical spatial frequency processor, whereas a short thesaurus listing various analogue quantities in these two systems is given in TABLE I. Particularly in (e), we show the field distribution in the image plane. The Fraunhofer diffraction pattern of the image is shown in (f), which is the Fourier transform of the field distribution of the image plane forming spatial frequency plane[27, 30] whereas in (g), the Fraunhofer diffraction pattern i.e., the Fourier transform of the spatial frequency plane is shown.

[49, 50]

$$\Psi_{\mathbf{k}}^{e,+}(\mathbf{r}) = \phi_{\mathbf{k}}^e(\vec{r}) - \frac{e^{i\mathbf{k}\mathbf{r}}}{2\hbar v_F} \sqrt{\frac{i\mathbf{k}}{\pi r}} \begin{bmatrix} 1 \\ e^{i\theta} \end{bmatrix} \langle \phi_{\mathbf{k}'}^e | \hat{T} | \phi_{\mathbf{k}}^e \rangle \quad (1)$$

where, transition operator $\hat{T} = \hat{V} + \hat{V} \hat{G}_0^\pm \hat{V} + \hat{V} \hat{G}_0^\pm \hat{V} \hat{G}_0^\pm \hat{V} + \dots$ and \hat{G}_0^\pm is the Green's function defined as $\hat{G}_0^\pm = \lim_{\epsilon \rightarrow 0} [E I_2 - \hat{H}_0 \pm i\epsilon]$. $(\phi_{\mathbf{k}}^{e,h})$ are respectively free particle electron and hole solutions of $\hat{H}_0 |\phi_{\mathbf{k}}\rangle = E |\phi_{\mathbf{k}}\rangle$. Here, \mathbf{k} is the wave-vector of the incident wave, $\mathbf{k}' = k\hat{r}$, θ is the angle between \mathbf{k} and \mathbf{k}' (see sec. I, SM[51]).

Realistic QD lattices that are heavily n-doped centres on a p-doped background[38–40] serves as scattering po-

tential V as a Gaussian quantum dot array

$$V(\mathbf{r}) = \sum_n \left(\frac{V_0}{2\pi\beta^2} \right) e^{-\frac{1}{2} \left(\frac{\mathbf{r}-\mathbf{r}_n}{\beta} \right)^2} \quad (2)$$

where \mathbf{r}_n are the centres of each quantum dot where the Gaussian potential of width β forms its maxima. Such potential profile can be created using a needle-like electrode offered by an STM tip [35–40], connected with a gate potential as shown in FIG. 1(a).

In experimental systems[35, 36, 38], these quantum dots are made on graphene/hBN heterostructures on SiO_2/Si substrate. The gate potential creates a stationary charge distribution in the insulating hBN underlayer, which creates the Gaussian potential profile

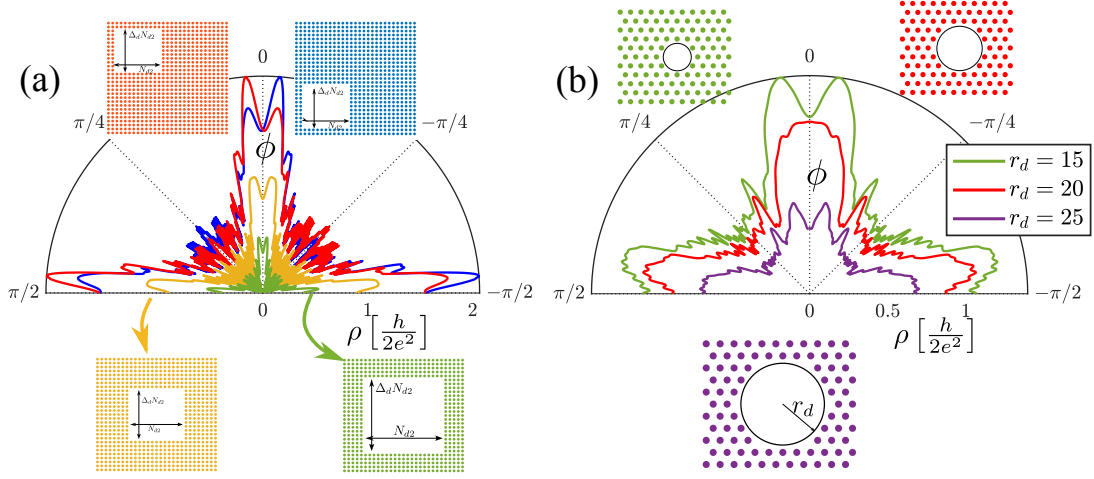


FIG. 2: Resistivity pattern for (a) square QD lattice of size $N_2 = 200$ and $\Delta = 1$ with square cavity with different sizes and (b) hexagonal QD lattice of size $N_2 = 61$ and $\Delta = 1$ with circular cavity of different radii. In (a), The resistivity pattern is symmetric on both sides of $\phi = 0$ only when the cavity is centred at the origin and for the blue curve, we have removed scatterers from $n_1 = 10$ to 110 and $n_2 = 10$ to 110 . For the orange curve $n_1 = 10$ to 110 and $n_2 = 90$ to 190 . In (b), the cavity is placed in the centre of the original QD lattice. Here, the resistivity pattern is symmetric on both sides of $\phi = 0$.

in the graphene sheet. The SiO_2/Si substrate acts as a global back gate. To make an array of such QDs, the single electrode can be replaced by an array of such electrodes[37, 52–55].

For the type of potential profile depicted in Eq. (2),

$$\frac{d\sigma}{d\theta} = \frac{1}{4\hbar^2 v_F^2} \left(\frac{k}{\pi} \right) V_0^2 \mu(\theta) M_1^2(\theta, \phi) M_2^2(\theta, \phi), \text{ square lattice with dimension } (\Delta N_2 \times N_2),$$

and hexagonal lattice rotated in an angle ϕ (3a)

$$= \frac{kV^2 \mu(\theta)}{4\pi \hbar^2 v_F^2} [M_1(N_2, \Delta, \phi, \mathbf{q}) M_2(N_2, \phi, \mathbf{q}) - M_1(N_{d2}, \Delta_d, \phi, \mathbf{q}) M_2(N_{d2}, \phi, \mathbf{q})]^2, \text{ square QD lattice with a ,}$$

cavity of rectangular shape (3b)

$$= \frac{kV^2 \mu(\theta)}{4\pi \hbar^2 v_F^2} \left[M_1 \left(N_2, \Delta, \phi - \frac{\delta}{2}, \mathbf{q} \right) M_2 \left(N_2, \phi - \frac{\delta}{2}, \mathbf{q} \right) + M_1 \left(N_2, \Delta, \phi + \frac{\delta}{2}, \mathbf{q} \right) M_2 \left(N_2, \phi + \frac{\delta}{2}, \mathbf{q} \right) \right]^2$$

moiré pattern of two QD lattices (3c)

Here, $M_1(N_2, \Delta, \phi, \mathbf{q}) = \frac{\sin(\frac{N_2 \Delta d}{2} \mathbf{q} \cdot \hat{x}')}{\sin(\frac{d}{2} \mathbf{q} \cdot \hat{x}')}$, $M_2(N_2, \phi, \mathbf{q}) = \frac{\sin(\frac{N_2 d}{2} \mathbf{q} \cdot \hat{y}')}{\sin(\frac{d}{2} \mathbf{q} \cdot \hat{y}')}$, are conventional Fraunhofer diffraction patterns for an one-dimensional grating in mutually transverse direction. $\mu(\theta) = (1 + \cos \theta) e^{-4k^2 \beta^2 \sin^2(\theta/2)}$ is due to the gaussian aperture profile (2) modulated by a factor due to the absence of backscattering [2, 47], and $\mathbf{q} = \mathbf{k} - \mathbf{k}'$, $\mathbf{r}_n = n_1 \hat{x}' + n_2 \hat{y}'$, where n_1 and n_2 are integers, and the x', y' axis is rotated with respect to the incident electrons by an angle ϕ . For the first case, we

the premise for Fourier electron optics(FEO) with such MDF can be developed first by evaluating differential scattering cross-sections (DSC), which we did for carefully chosen three prototype combinations of such dot lattices and subsequently demonstrating their effect on transport. The DSCs evaluated respectively are:

take QDs arranged in square and hexagonal lattice arrangement with suitable choices of \mathbf{r}_n . The corresponding result, which is plotted in FIG. 1(b) in a polar plot, mimics the well-known Fraunhofer pattern with suitable modification due to the absence of back-scattering. This can be thought of as a two-dimensional generalisation of the well-known result of scattering by a smooth p-n junction in one dimension[1], $T \sim \exp(-\pi k_F \beta \sin^2(\theta)/2)$, as the scattering decreases exponentially with β in Eq. (3a) as $\frac{d\sigma}{d\theta} \sim e^{-4k^2 \beta^2 \sin^2(\theta/2)}$ with a characteristic length(β in our case). The comparison with the corresponding cases

TABLE I: Dictionary for various quantities in Fraunhofer diffraction in optics and their counterparts in scattering of MDF in graphene from a QD lattice:

Fraunhofer Diffraction in optics	Scattering of MDF in graphene from QD lattice
Aperture profile $A(\mathbf{r}')$	Scattering potential $V(\mathbf{r}')$
Field distribution at diffraction plane $G(u, v) = \frac{1}{\lambda f} \iint dx' dy' g(x', y') e^{-i(ux' + vy')}$	Scattering amplitude $f(\theta) = -\sqrt{\frac{ik}{2\pi}} \frac{(1+e^{i\theta})}{2hv_F} \iint dx' dy' V(x', y') e^{i(q_x x' + q_y y')}$
Intensity $I = G(x, y) ^2$	Differential Scattering cross section $\frac{d\sigma}{d\theta} = f(\theta) ^2$
$u = \frac{2\pi x}{\lambda f}$ and $v = \frac{2\pi y}{\lambda f}$	$-q_x$ and $-q_y$
$\frac{1}{\lambda f}$	$-\frac{1}{2hv_F} \sqrt{\frac{ik}{2\pi}} (1 + e^{-i\theta})$
$\left(\frac{2\pi}{\lambda f}\right) \mathbf{r}$	$-\mathbf{q} = \mathbf{k}' - \mathbf{k}$
$\left(\frac{2\pi}{\lambda f}\right)^2 r^2$	$q^2 = 4k^2 \sin^2\left(\frac{\theta}{2}\right)$

of non-relativistic charge carriers is discussed in [51].

In the next two cases, we first consider a scattering lattice made of TDQDL with cavities of different shapes and sizes (Eq. (3b), FIG. 2), and then a third case of scattering potential made with moiré pattern of two square lattices of TDQDL (FIG. 3), making the differential scattering cross-section dependent on the twist angle(δ) between the two square TDQDLs. The scattering amplitude for the TDQDL with a cavity is the difference between the contribution from the original TDQDL scattering potential (without the cavity) and a TDQDL of the same shape and position of the cavity in Eq. (3b). In the third case of moiré pattern, the scattering amplitude is again the sum of the contributions from two lattices rotated with respect to each other, and the differential scattering cross section in Eq. (3c) is the square of this sum. This happens due to the linearity property of the Fourier transform[31]. In the analogous case of optical diffraction systems, this is known as Babinet's principle[31, 56, 57].

For the square TDQDL with cavity, we have considered four specific cases by varying the locations and sizes of the cavities. For a square cavity($\Delta_d = 1$) in a square TDQDL, the length of the side of the square-shaped cavities(N_{d2}) is varied to vary the size of the cavities. We have also taken two cases where the centre of the cavity does not coincide with the centre of the parent square TDQDL. For the moiré pattern, the moiré lattice vector d_M is related to the twist angle by $\delta = 2 \sin^{-1}\left(\frac{d}{2d_M}\right)$ [58]. The Bragg condition for the first two cases in Eq. (3a) and (3b) is given by $k^2 d^2 \sin^2\left(\frac{\theta}{2}\right) = (n_1^2 + n_2^2)\pi^2$, where n_1 and n_2 are integers (see FIG. S2 in sec. III of SM[51]).

The moiré pattern produces a periodic pattern with lattice periodicities $\sqrt{2}Nd_M$ [58, 59] for the commensurate angles where N is an integer. The commensurate super-cell lattice vectors [60, 61] for $\phi = 0$ are given by $\mathbf{R}_{C1} = \left(\frac{d}{2\sin(\delta/2)}\right) N(\hat{x} + \hat{y})$ and $\mathbf{R}_{C2} = \left(\frac{d}{2\sin(\delta/2)}\right) N(-\hat{x} + \hat{y})$

For every value of N , we get a set of commensurate angles. For the particular commensurate structure that we have considered for square lattice, this common pe-

riod is larger than the moiré cell by factor $\sqrt{2}$ [58] (see FIG. 3(c)). The moiré lattice with lattice periodicity d_M is shown in green. This commensurate lattice is shown in black in FIG. 3(c). The primitive lattice vectors \mathbf{R}_{C1} and \mathbf{R}_{C2} are not same as the moiré lattice vectors $\mathbf{R}_{M1} = \left(\frac{d}{2\sin(\delta/2)}\right) \hat{x}$ and $\mathbf{R}_{M2} = \left(\frac{d}{2\sin(\delta/2)}\right) \hat{y}$. Due to the commensurate periodicity, scattering potentials made with such patterns show additional Bragg condition from Eq. (3c),

$$2Nk^2 d_M^2 \sin^2\left(\frac{\theta}{2}\right) = (m_1^2 + m_2^2) \quad (4)$$

The detailed discussion on the maximum scattering conditions is sec. III of SM[51].

To understand how the above results can be interpreted as an electronics analogue of Fourier optics in a succinct way, in the left column of TABLE I we list quantities that characterise a Fraunhofer diffraction-based spatial frequency filtering in optical imaging systems[27, 29, 30] and are demonstrated in FIG. 1 (e), (f), (g). In the right column of the same table, we list the corresponding quantities that define the analogue system of MDF scattered by a QD lattice. From TABLE I, we can observe that both the scattering amplitude in our system, $f(\theta)$ and the amplitude distribution at the spatial frequency plane in FIG. 1(e), $G(u, v)$ is the Fourier transform of the scattering potential $V(x', y')$ and the object distribution $g(x', y')$ respectively, whereas the presence of $(1 + e^{i\theta})$ term in $f(\theta)$ of MDF indicates the absence of backscattering[2, 5, 47]. For MDF, the position coordinate (\mathbf{r}) is transformed to angular wave number coordinate (\mathbf{q}), whereas in the corresponding optical system, the coordinates of the plane of aperture, x' and y' , are transformed to u and v , respectively. Correspondingly, the differential cross section, $\frac{d\sigma}{d\theta}$ in the case of MDF is replaced by intensity distribution I in the optical case as demonstrated in FIG. 1(b) and (f),

A noteworthy difference with the corresponding optical system appears when the superposition of two such TDQDL, rotated with respect to each other so that the resulting pattern is a moiré pattern, widely studied in

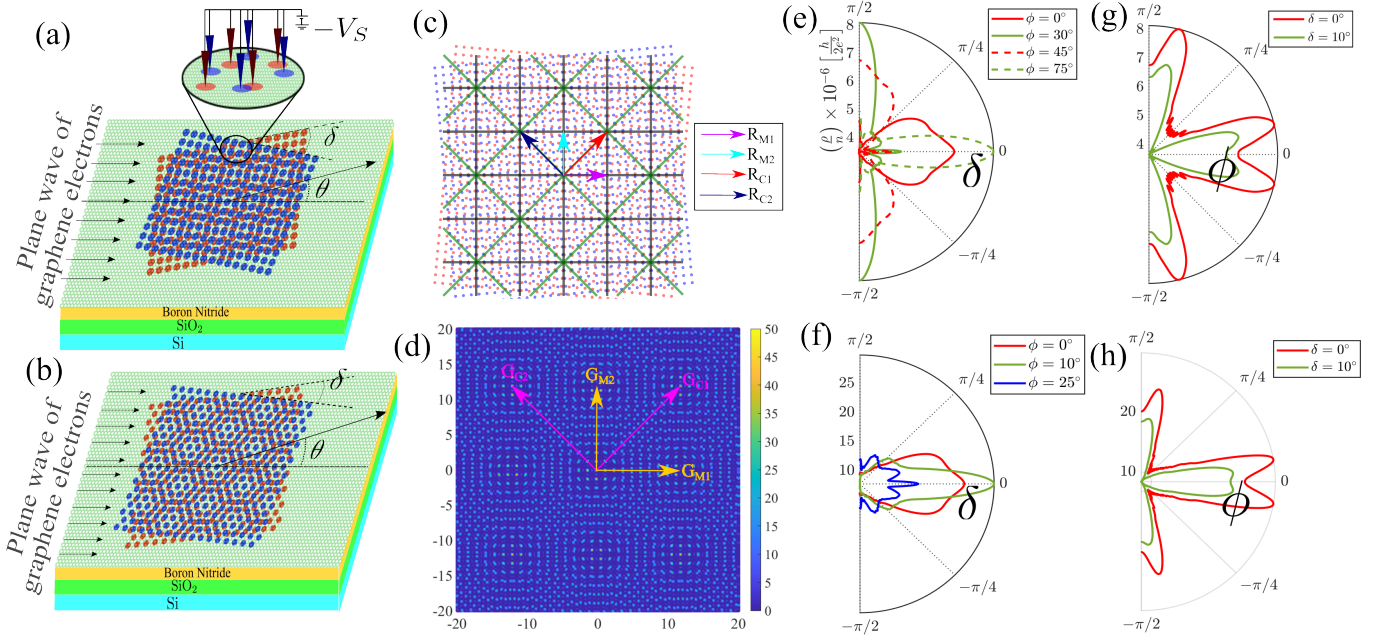


FIG. 3: The schematic diagram of a plane wave of massless Dirac fermions getting scattered by a moiré superlattice of two (a) square and (b) hexagonal lattices of Gaussian quantum dots(QD) in graphene. Moiré pattern made by two square lattices of TDQDL producing a commensurate structure at a twist angle, $\delta \approx 6.026^\circ$ is shown in (c). The moiré lattice is shown in green, and the commensurate lattice is shown in black. The creation of such quantum dots by using tips with applied gate voltage in the same way as in FIG. 1. In (d) $|\tilde{V}(\mathbf{q}_1)|^2$ is plotted as a function of q_{1x} and q_{1y} for the above scattering potential. The resistivity pattern with the mean angle(ϕ) is shown in (e) and (f) for a TDQDL scattering potential made with moiré pattern of two square and hexagonal lattices, respectively. In (g) and (h), the resistivity pattern is plotted with the twist angle(δ) again for a moiré pattern of two square and hexagonal lattices, respectively.

optics[15, 62–64] and condensed matter[60, 61, 65–69]. Such moiré patterns are studied in optical imaging to improve the microscope’s imaging capabilities in Structural Imaging Microscopy [70–72]. However whereas in optical systems the resultant aperture profile becomes $g_1(x', y') \times g_2(x', y')$ [73, 74] for two transparencies $g_{1,2}$, making the aperture plane consists of two transparencies $g_1(x', y')$ and $g_2(x', y')$, leading to the new pattern consists of new beating frequencies [75], for MDF scattered by two potentials $V_1(x', y')$ and $V_2(x', y')$, the differential scattering cross section depends on the Fourier transform of $V_1(x', y') + V_2(x', y')$ leading to additional maximum scattering conditions from Eq. (3c) shown in Eq. (4) and depicted in FIG. 3 (d). The resultant scattering potential shows a new periodicity only for commensurate angles.

The above analogy between the scattering problem of MDF from TDQDL and the Fourier optics using a 2D grating naturally leads to the question if this can be extended to the electronic analogue of image processing in the optical case, which is achieved through a second FT through lenses in the optical system (see FIG. 1(g)). Whereas a direct analogy is difficult, we show here that selected information about the structure of the TDQDL can be retrieved by rotating our scattering po-

tential about a transverse axis passing through the centre of the TDQDL, thereby introducing a spatial angle ϕ between the propagation direction of the MDF and the symmetry axis with respect to the incident plane wave to introduce another degree of freedom, and evaluating the dc resistivity at zero temperature is[76, 77] using the semi-classical Boltzmann theory by

$$\rho = \frac{2nv_F\sigma_{tr}}{e^2v_F^2D(E_F)} = \frac{2n}{e^2v_FD(E_F)} \int_0^{2\pi} d\theta (1 - \cos\theta) \frac{d\sigma}{d\theta}. \quad (5)$$

We note that is valid in the limit of small concentration (n) of external potential centres, Here, e =charge of an electron, v_F = Fermi velocity, $D(E_F)$ = density of states at Fermi energy (variation of resistivity with E_F is discussed in FIG. S3 of sec. IV in SM[51]), $\tau(k_F) = (nv_F\sigma_{tr})^{-1}$ is the transport relaxation time(at the Fermi surface) or the mean free path time and σ_{tr} is the transport scattering cross-section. Corresponding values of the resistivities in systems considered are within the typical range of observed resistivities in graphene-based systems[78–80]. Additionally, our calculated values of resistivities can also be adjusted by choosing the gate voltages applied at every QD and varying the height

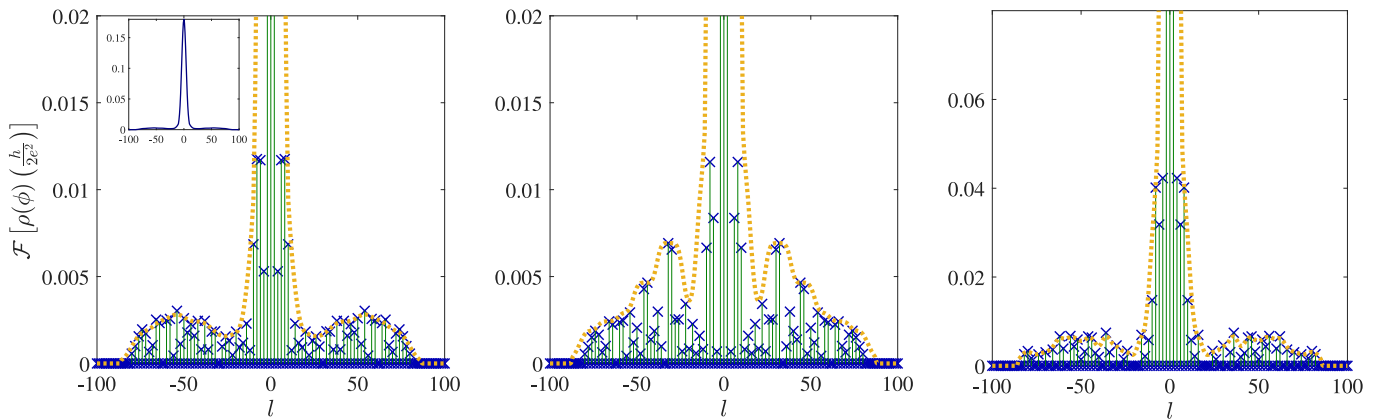


FIG. 4: (a) Shows the Fourier transform(FT) of the resistivity pattern for a TDQDL with $N_2 = 50$, $\Delta = 1$ and $d = 70$ (nm). The blue cross (\times) denotes the value of amplitude corresponding to each spatial frequency (l). In the inset, we have shown the total data. The main figures do not show the central peak to display the smaller values. The FT of the resistivity pattern through a Gaussian filter for the same TDQDL scattering potential with a square cavity (in the centre) is shown in (b). In (c), we show the FT of the resistivity pattern through a Gaussian filter for a scattering potential made with a moiré pattern of two square TDQDL with the same lattice constant.

of the scatterers.

The corresponding results, namely the angular distribution of resistivity, are plotted in FIG. 1(c) and (d) for square and hexagonal TDQDL, in FIG. 2(a) and (b) for TDQDL with a cavity, and in FIG. 3 (e),(f),(g) and (h) for moiré pattern of two TDQDL lattices, to demonstrate how certain structural information of these TDQDLs can be retrieved from this angle-resolved resistivity.

We begin with the observation that $\rho(\phi)$ in FIG. 1(c) and (d) reflects the discrete rotational symmetry of the square and hexagonal lattice, e.g. $\left. \frac{d\sigma}{d\theta} \right|_{\Delta, N_2, \phi=0^\circ} = \left. \frac{d\sigma}{d\theta} \right|_{\frac{1}{\Delta}, \Delta N_2, \phi=90^\circ}$ in case for square lattice, but not for the hexagonal lattice. This may be contrasted with the observation in FIG. 1(c) and (d) that $\rho(-\pi/2) = \rho(\pi/2)$ for both square and hexagonal lattice of TDQDL. For TDQDL with a cavity, the resistivity pattern calculated with the help of Eq. (3b) and Eq. (5) reveals both the symmetry of the TDQDL, as well as the location and size of the cavity. In FIG. 2(a) comparing between blue, red, and orange-yellow plots of the $\rho(\phi)$, we see that the location of the square cavity in the corresponding square TDQDL indeed exhibits itself in the symmetry of the resistivity plot about the $\phi = 0$ line. Similarly, comparing the cases of orange-yellow and the green plots of $\rho(\phi)$, we see that the size of the cavity, which is proportional to the number of removed scattering centres, indeed effect the magnitude of the resistivity pattern. Hexagonal TDQDL, with cavities of circular shape with radius(r_d) in FIG. 2(b), shows the same effect(see FIG. S4 and S5 in sec. V of SM[51]). The differential scattering cross section for the scattering potential made with a moiré pattern of two square lattices of TDQDL is shown in Eq. (3c). In FIG. 3 (d), we show $\tilde{V}(\mathbf{q})$ as a function of q_{1x} and q_{1y} [51]. As expected, FT is also a moiré pattern

of two square patterns in inverse space but multiplied by the same $\mu(\theta)$ given in Eq. (3c). In FIG. 3, (e), we show the dependence of the resistivity pattern on the twist angle(δ) for fixed values of average angle (ϕ) with the incident plane wave of massless Dirac fermions.

The most prominent features of these resistivity plots of TDQDL in FIG. 1(c) and (d), for TDQDL with cavities in FIG. 2(a), and (b), and for moiré pattern of TDQDLs in FIG. 3(e)-(h), are oscillations in resistivity as a function of the angular variable (see FIG. S6 in sec. VI, SM[51]). To understand the oscillations in resistivity plots FIG. 1(c) and (d) in a more quantitative way we did an FT of the resistivity that can provide the range of these angular frequencies (see FIG. 4). If we choose l as the conjugate variable of ϕ , we can denote the highest angular frequency component present in one ρ vs ϕ curve as l_c or cut-off angular frequency for a given lattice(see FIG. S7 in sec. VII of SM[51]). In FIG. 4 (a), the Fourier spectrum of the resistivity pattern as a function of l for a TDQDL shows a feature that is similar to the side-band formation. We highlight this aspect through an envelope function (dotted orange curve) over the actual result. For the same TDQDL, with a cavity at the centre, and for the same cut-off frequency, this side-band like feature becomes more prominent in FIG. 4 (b), whereas this side-band like feature gets highly suppressed in the case of moiré pattern of two relatively twisted TDQDLs in FIG. 4(c). These points out that certain angular frequency components get enhanced or suppressed as the scattering region is removed or added, a phenomenon akin to the spatial frequency filtering in Fourier optics, but now happening in the solid state environment for the angle-resolved resistivity, a transport coefficient. This can also be linked to the electronic analogue of Babinet's principle that we reported earlier in this manuscript. Establishing the electronic analogue of Babinet's principle

and the consequent spatial frequency filtering in the evaluated angle resolved resistivity in the ballistic transport regime of MDF scattered from TDQDL, thus forming the most prominent findings in this work.

To summarize, using the Lippmann-Schwinger formalism, we established an electronic analogue of Fourier optics i.e., FEO by mapping the scattering cross-section of MDF from TDQDLs to the Fraunhofer diffraction pattern and providing a dictionary of such mapping. By considering TDQDL with cavity and moiré pattern of such TDQDLs, we demonstrated an electronic analogue of Babinet's principle. Harnessing this analogy further with an eye on practical application, we evaluated the

angle-resolved resistivity of these scattered MDs, and Fourier analyze the same to show that the Fourier spectrum shows spatial frequency filtering consistent with Babinet's principle. With the quantum dot arrays now routinely produced in semiconductor-based systems[52–54], we hope our proposed analogy can be used for making new electronic devices based on such analogue FEO.

We thank Kedar Khare, Rohit Narula and Deepanshu Aggarwal for the helpful discussions. SG and RM are supported by a SPARC Phase II (MHRD, GOI, Project Code P2117) grant, whereas PSB is supported by a MHRD Fellowship.

-
- [1] V. V. Cheianov and V. I. Fal'ko, Selective transmission of dirac electrons and ballistic magnetoresistance of $n-p$ junctions in graphene, *Phys. Rev. B* **74**, 041403 (2006).
- [2] M. Katsnelson, K. Novoselov, and A. Geim, Chiral tunnelling and the klein paradox in graphene, *Nat. Phys.* **2**, 620 (2006).
- [3] V. V. Cheianov, V. Fal'ko, and B. L. Altshuler, The focusing of electron flow and a veselago lens in graphene $p-n$ junctions, *Science* **315**, 1252 (2007).
- [4] A. F. Young and P. Kim, Quantum interference and klein tunnelling in graphene heterojunctions, *Nature Physics* **5**, 222 (2009).
- [5] N. Stander, B. Huard, and D. Goldhaber-Gordon, Evidence for klein tunneling in graphene $p-n$ junctions, *Phys. Rev. Lett.* **102**, 026807 (2009).
- [6] S. Chen, Z. Han, M. M. Elahi, K. M. M. Habib, L. Wang, B. Wen, Y. Gao, T. Taniguchi, K. Watanabe, J. Hone, A. W. Ghosh, and C. R. Dean, Electron optics with $p-n$ junctions in ballistic graphene, *Science* **353**, 1522 (2016).
- [7] J. B. Pendry, Negative refraction makes a perfect lens, *Phys. Rev. Lett.* **85**, 3966 (2000).
- [8] D. Schurig, J. J. Mock, B. J. Justice, S. A. Cummer, J. B. Pendry, A. F. Starr, and D. R. Smith, Metamaterial electromagnetic cloak at microwave frequencies, *Science* **314**, 977 (2006).
- [9] G.-H. Lee, G.-H. Park, and H.-J. Lee, Observation of negative refraction of dirac fermions in graphene, *Nat. Phys.* **11**, 925 (2015).
- [10] B. Brun, N. Moreau, S. Somanchi, V.-H. Nguyen, K. Watanabe, T. Taniguchi, J.-C. Charlier, C. Stampfer, and B. Hackens, Imaging dirac fermions flow through a circular veselago lens, *Phys. Rev. B* **100**, 041401 (2019).
- [11] S. Tchoumakov, J. Cayssol, and A. G. Grushin, Three-dimensional chiral veselago lensing, *Phys. Rev. B* **105**, 075309 (2022).
- [12] X. Zhang, W. Ren, E. Bell, Z. Zhu, K.-T. Tsai, Y. Luo, K. Watanabe, T. Taniguchi, E. Kaxiras, M. Luskun, *et al.*, Gate-tunable veselago interference in a bipolar graphene microcavity, *Nat Commun* **13**, 6711 (2022).
- [13] P. Bøggild, J. M. Caridad, C. Stampfer, G. Calogero, N. R. Papior, and M. Brandbyge, A two-dimensional dirac fermion microscope, *Nat. Commun.* **8**, 15783 (2017).
- [14] C.-H. Park, Y.-W. Son, L. Yang, M. L. Cohen, and S. G. Louie, Electron beam supercollimation in graphene superlattices, *Nano Letters* **8**, 2920 (2008).
- [15] M.-H. Liu, C. Gorini, and K. Richter, Creating and steering highly directional electron beams in graphene, *Phys. Rev. Lett.* **118**, 066801 (2017).
- [16] K. Wang, M. M. Elahi, L. Wang, K. M. Habib, T. Taniguchi, K. Watanabe, J. Hone, A. W. Ghosh, G.-H. Lee, and P. Kim, Graphene transistor based on tunable dirac fermion optics, *Proc. Natl. Acad. Sci. U.S.A.* **116**, 6575 (2019).
- [17] D. S. Wei, T. van der Sar, J. D. Sanchez-Yamagishi, K. Watanabe, T. Taniguchi, P. Jarillo-Herrero, B. I. Halperin, and A. Yacoby, Mach-zehnder interferometry using spin-and valley-polarized quantum hall edge states in graphene, *Sci. Adv.* **3**, e1700600 (2017).
- [18] M. Jo, P. Brasseur, A. Assouline, G. Fleury, H.-S. Sim, K. Watanabe, T. Taniguchi, W. Dumnernpanich, P. Roche, D. C. Glatli, N. Kumada, F. D. Parmentier, and P. Roulleau, Quantum hall valley splitters and a tunable mach-zehnder interferometer in graphene, *Phys. Rev. Lett.* **126**, 146803 (2021).
- [19] P. Rickhaus, R. Maurand, M.-H. Liu, M. Weiss, K. Richter, and C. Schönenberger, Ballistic interferences in suspended graphene, *Nat. Commun.* **4**, 2342 (2013).
- [20] G. Forghieri, P. Bordone, and A. Bertoni, Time-dependent transport in graphene mach-zehnder interferometers, *Phys. Rev. B* **106**, 165402 (2022).
- [21] P. Rickhaus, P. Makk, M.-H. Liu, K. Richter, and C. Schönenberger, Gate tuneable beamsplitter in ballistic graphene, *Appl. Phys. Lett.* **107**, 251901 (2015).
- [22] C. Handschin, P. Makk, P. Rickhaus, M.-H. Liu, K. Watanabe, T. Taniguchi, K. Richter, and C. Schönenberger, Fabry-pérot resonances in a graphene/hbn moiré superlattice, *Nano letters* **17**, 328 (2017).
- [23] E. Paredes-Rocha, Y. Betancur-Ocampo, N. Szipak, and T. Stegmann, Gradient-index electron optics in graphene $p-n$ junctions, *Phys. Rev. B* **103**, 045404 (2021).
- [24] R. L. Heinisch, F. X. Bronold, and H. Fehske, Mie scattering analog in graphene: Lensing, particle confinement, and depletion of klein tunneling, *Phys. Rev. B* **87**, 155409 (2013).
- [25] R. N. Sajjad, S. Sutar, J. U. Lee, and A. W. Ghosh, Manifestation of chiral tunneling at a tilted graphene $p-n$ junction, *Phys. Rev. B* **86**, 155412 (2012).
- [26] F. Anwar, A. Iurov, D. Huang, G. Gumbs, and A. Sharma, Interplay between effects of barrier tilting

- and scatterers within a barrier on tunneling transport of dirac electrons in graphene, *Phys. Rev. B* **101**, 115424 (2020).
- [27] K. Birch, A spatial frequency filter to remove zero frequency, *Opt. Acta.* **15**, 113 (1968).
- [28] A. Ghatak, *Optics* (Tata McGraw-Hill Publishing Company Limited, 2009).
- [29] J. Goodman, *Introduction to Fourier Optics*, McGraw-Hill physical and quantum electronics series (W. H. Freeman, 2005).
- [30] K. G. Birch, Spatial filtering in optical data-processing, *Rep. Prog. Phys.* **35**, 1265 (1972).
- [31] M. Born and E. Wolf, *Principles of Optics: Electromagnetic Theory of Propagation, Interference and Diffraction of Light (7th Edition)*, 7th ed. (Cambridge University Press, 1999).
- [32] F. Jenkins and H. White, *Fundamentals of Optics*, International student edition (McGraw-Hill, 1976).
- [33] P. Silvestrov and K. Efetov, Quantum dots in graphene, *Phys. Rev. Lett.* **98**, 016802 (2007).
- [34] D. Joung, L. Zhai, and S. I. Khondaker, Coulomb blockade and hopping conduction in graphene quantum dots array, *Phys. Rev. B* **83**, 115323 (2011).
- [35] F. Ghahari, D. Walkup, C. Gutiérrez, J. F. Rodriguez-Nieva, Y. Zhao, J. Wyrick, F. D. Natterer, W. G. Cullen, K. Watanabe, T. Taniguchi, L. S. Levitov, N. B. Zhitenev, and J. A. Stroscio, An on/off berry phase switch in circular graphene resonators, *Science* **356**, 845 (2017).
- [36] C. Gutiérrez, D. Walkup, F. Ghahari, C. Lewandowski, J. F. Rodriguez-Nieva, K. Watanabe, T. Taniguchi, L. S. Levitov, N. B. Zhitenev, and J. A. Stroscio, Interaction-driven quantum hall wedding cake like structures in graphene quantum dots, *Science* **361**, 789 (2018).
- [37] H. V. Grushevskaya, G. G. Krylov, S. P. Kruchinin, B. Vlahovic, and S. Bellucci, Electronic properties and quasi-zero-energy states of graphene quantum dots, *Phys. Rev. B* **103**, 235102 (2021).
- [38] J. Lee, D. Wong, J. Velasco Jr, J. F. Rodriguez-Nieva, S. Kahn, H.-Z. Tsai, T. Taniguchi, K. Watanabe, A. Zettl, F. Wang, *et al.*, Imaging electrostatically confined dirac fermions in graphene quantum dots, *Nature Phys.* **12**, 1032 (2016).
- [39] Y. Zhao, J. Wyrick, F. D. Natterer, J. F. Rodriguez-Nieva, C. Lewandowski, K. Watanabe, T. Taniguchi, L. S. Levitov, N. B. Zhitenev, and J. A. Stroscio, Creating and probing electron whispering-gallery modes in graphene, *Science* **348**, 672 (2015).
- [40] S.-Y. Li and L. He, Recent progresses of quantum confinement in graphene quantum dots, *Front. Phys.* **17**, 1 (2022).
- [41] K. S. Novoselov, A. K. Geim, S. V. Morozov, D.-e. Jiang, Y. Zhang, S. V. Dubonos, I. V. Grigorieva, and A. A. Firsov, Electric field effect in atomically thin carbon films, *Science* **306**, 666 (2004).
- [42] A. C. Neto, F. Guinea, N. M. Peres, K. S. Novoselov, and A. K. Geim, The electronic properties of graphene, *Rev. Mod. Phys.* **81**, 109 (2009).
- [43] S. Bhandari, G. H. Lee, K. Watanabe, T. Taniguchi, P. Kim, and R. M. Westervelt, Imaging electron flow from collimating contacts in graphene, *2D Materials* **5**, 021003 (2018).
- [44] C. Gutiérrez, L. Brown, C.-J. Kim, J. Park, and A. N. Pasupathy, Klein tunnelling and electron trapping in nanometre-scale graphene quantum dots, *Nature Physics* **12**, 1069 (2016).
- [45] S. Bhandari, G.-H. Lee, A. Klales, K. Watanabe, T. Taniguchi, E. Heller, P. Kim, and R. M. Westervelt, Imaging cyclotron orbits of electrons in graphene, *Nano Letters* **16**, 1690 (2016), PMID: 26845290.
- [46] J. Berezovsky and R. M. Westervelt, Imaging coherent transport in graphene (part ii): probing weak localization, *Nanotechnology* **21**, 274014 (2010).
- [47] P. E. Allain and J.-N. Fuchs, Klein tunneling in graphene: optics with massless electrons, *Eur. Phys. J. B* **83**, 301 (2011).
- [48] C. Dartora, F. Zanella, and G. Cabrera, The theory for a 2d electron diffractometer using graphene, *J. Appl. Phys.* **132**, 124305 (2022).
- [49] J. J. Sakurai, *Modern quantum mechanics*, rev. ed ed. (Addison-Wesley Pub. Co, 1994).
- [50] S. K. Adhikari, Quantum scattering in two dimensions, *Am. J. Phys.* **54**, 362 (1986).
- [51] See Supplemental Material, for the details about Lippmann-Schwinger formalism in Sec. I, the comparison of scattering in 2DES and graphene in sec. II, a maximum scattering condition in sec. III, dependence of resistivity pattern on Fermi energy in sec. IV, the dependence of size and shape of the cavity on the resistivity pattern in sec. V, discussion about oscillations in the resistivity pattern in sec. VI, Fourier analysis of the resistivity pattern in sec. VII.
- [52] X. Wang, E. Khatami, F. Fei, J. Wyrick, P. Namboodiri, R. Kashid, A. F. Rigosi, G. Bryant, and R. Silver, Experimental realization of an extended fermi-hubbard model using a 2d lattice of dopant-based quantum dots, *Nat Commun* **13**, 6824 (2022).
- [53] D. Schröer, A. D. Greentree, L. Gaudreau, K. Eberl, L. C. L. Hollenberg, J. P. Kotthaus, and S. Ludwig, Electrostatically defined serial triple quantum dot charged with few electrons, *Phys. Rev. B* **76**, 075306 (2007).
- [54] T. Hensgens, T. Fujita, L. Janssen, X. Li, C. Van Diepen, C. Reichl, W. Wegscheider, S. Das Sarma, and L. M. Vandersypen, Quantum simulation of a fermi-hubbard model using a semiconductor quantum dot array, *Nature* **548**, 70 (2017).
- [55] J. Salfi, J. Mol, R. Rahman, G. Klimeck, M. Simmons, L. Hollenberg, and S. Rogge, Quantum simulation of the hubbard model with dopant atoms in silicon, *Nat Commun* **7**, 11342 (2016).
- [56] J. Babinet, *Mémoires d'optique météorologique*, Vol. 4 (1837) pp. 638–648.
- [57] J. R. Jiménez and E. Hita, Babinet's principle in scalar theory of diffraction, *Optical Review* **8**, 495 (2001).
- [58] A. Dunbrack and J. Cano, Intrinsically multilayer moiré heterostructures, *Phys. Rev. B* **107**, 235425 (2023).
- [59] O. Can, T. Tummuru, R. P. Day, I. Elfimov, A. Damascelli, and M. Franz, High-temperature topological superconductivity in twisted double-layer copper oxides, *Nature Physics* **17**, 519 (2021).
- [60] J. M. B. Lopes dos Santos, N. M. R. Peres, and A. H. Castro Neto, Graphene bilayer with a twist: Electronic structure, *Phys. Rev. Lett.* **99**, 256802 (2007).
- [61] S. Carr, S. Fang, and E. Kaxiras, Electronic-structure methods for twisted moiré layers, *Nature Reviews Materials* **5**, 748 (2020).
- [62] R. Bracewell, *Two-dimensional Imaging*, Prentice-Hall signal processing series (Prentice Hall, 1995).

- [63] E. Bar-Ziv, Effect of diffraction on the moiré image. i. theory, *J. Opt. Soc. Am. A* **2**, 371 (1985).
- [64] A. A. Ushkov, I. Verrier, T. Kampfe, and Y. Jourlin, Subwavelength diffraction gratings with macroscopic moiré; patterns generated via laser interference lithography, *Opt. Express* **28**, 16453 (2020).
- [65] R. Bistritzer and A. H. MacDonald, Moiré bands in twisted double-layer graphene, *Proceedings of the National Academy of Sciences* **108**, 12233 (2011).
- [66] K. Kim, A. DaSilva, S. Huang, B. Fallahazad, S. Larentis, T. Taniguchi, K. Watanabe, B. J. LeRoy, A. H. MacDonald, and E. Tutuc, Tunable moiré bands and strong correlations in small-twist-angle bilayer graphene, *Proceedings of the National Academy of Sciences* **114**, 3364 (2017).
- [67] H. Yoo, R. Engelke, S. Carr, S. Fang, K. Zhang, P. Cazeaux, S. H. Sung, R. Hovden, A. W. Tsen, T. Taniguchi, K. Watanabe, G.-C. Yi, M. Kim, M. Luskin, E. B. Tadmor, E. Kaxiras, and P. Kim, Atomic and electronic reconstruction at the van der waals interface in twisted bilayer graphene, *Nature Materials* **18**, 448 (2019).
- [68] G. Tarnopolsky, A. J. Kruchkov, and A. Vishwanath, Origin of magic angles in twisted bilayer graphene, *Phys. Rev. Lett.* **122**, 106405 (2019).
- [69] D. Aggarwal, R. Narula, and S. Ghosh, A primer on twistronics: a massless dirac fermion’s journey to moiré patterns and flat bands in twisted bilayer graphene, *Journal of Physics: Condensed Matter* **35**, 143001 (2023).
- [70] M. Saxena, G. Eluru, and S. S. Gorthi, Structured illumination microscopy, *Adv. Opt. Photon.* **7**, 241 (2015).
- [71] F. Ströhl and C. F. Kaminski, Frontiers in structured illumination microscopy, *Optica* **3**, 667 (2016).
- [72] A. Classen, J. von Zanthier, M. O. Scully, and G. S. Agarwal, Superresolution via structured illumination quantum correlation microscopy, *Optica* **4**, 580 (2017).
- [73] S. Zhou, Y. Fu, X. Tang, S. Hu, W. Chen, and Y. Yang, Fourier-based analysis of moiré fringe patterns of superposed gratings in alignment of nanolithography, *Opt. Express* **16**, 7869 (2008).
- [74] L. Kong, S. Cai, Z. Li, G. Jin, S. Huang, K. Xu, and T. Wang, Interpretation of moiré phenomenon in the image domain, *Opt. Express* **19**, 18399 (2011).
- [75] O. Bryngdahl, Moiré: Formation and interpretation, *J. Opt. Soc. Am.* **64**, 1287 (1974).
- [76] T. M. Radchenko, A. A. Shylau, I. V. Zozoulenko, and A. Ferreira, Effect of charged line defects on conductivity in graphene: Numerical kubo and analytical boltzmann approaches, *Phys. Rev. B* **87**, 195448 (2013).
- [77] A. Ferreira, J. Viana-Gomes, J. Nilsson, E. R. Mucciolo, N. M. R. Peres, and A. H. Castro Neto, Unified description of the dc conductivity of monolayer and bilayer graphene at finite densities based on resonant scatterers, *Phys. Rev. B* **83**, 165402 (2011).
- [78] J.-H. Chen, C. Jang, S. Xiao, M. Ishigami, and M. S. Fuhrer, Intrinsic and extrinsic performance limits of graphene devices on SiO₂, *Nature Nanotech* **3**, 206 (2008).
- [79] O. Balci and C. Kocabas, Rapid thermal annealing of graphene-metal contact, *Applied Physics Letters* **101**, 243105 (2012).
- [80] F. Giubileo and A. Di Bartolomeo, The role of contact resistance in graphene field-effect devices, *Progress in Surface Science* **92**, 143 (2017).